

INTENSE ELECTRON BEAM DISRUPTION DUE TO ION RELEASE FROM SURFACES

C. Vermare, H. A. Davis, T. P. Hughes, D. C. Moir, R. T. Olson and W. M. Wood
Los Alamos National Laboratory, Los Alamos, NM, USA

Abstract

A major concern for the DARHT second axis (2 kA, 18.6 MeV, 2000 ns) is that ions or ionized neutrals released from solid surfaces (e.g., apertures, septum, dumps, and targets) by beam impact can be accelerated and trapped by the beam potential. This positive charge will be electrically attracted to the beam and could disrupt it. Possible release mechanisms include electron induced desorption of neutrals or ions, thermal desorption due to target heating and melting or vaporization of the solid target. To study this, experiments were performed on the DARHT first axis. Here, the beam, focused to a range of diameters, is transmitted through thin foils made of various materials. The time-dependent beam radial profile is measured downstream of the target. For low current density (depending on the material used), the downstream-beam profile is time invariant as expected. At higher current density, the downstream-beam radius changes during the pulse followed by transverse instability. Data, particle-in-cell simulations, and comparisons are presented.

1 INTRODUCTION

The Dual-Axis Radiographic Hydrodynamics Testing (DARHT) facility will use two perpendicular electron Linear Induction Accelerators (LIA) to produce intense, bremsstrahlung x-ray pulses for flash radiography of dense objects. The first axis, already operational, produces a single electron pulse with 1.7 kA current, 19.8 MeV energy and 60 ns pulse duration. The second axis, under construction, will generate a 2.0 kA, 19.8 MeV, 2000 ns beam. A sequence of four shorter-duration pulses from this beam will be delivered to the x-ray converter by a fast kicker system. The second axis differs from previous LIA's by its much longer pulse duration, typically 10-20 times longer.

This longer pulse can allow a number of deleterious phenomena that are not critical on shorter pulse LIA's. Among these is the beam-induced release of ions or neutrals subsequently ionized by the beam. Ions created at a surface by beam impact, will be accelerated and trapped in the beam channel. These ions will partially neutralize the beam space charge upsetting its equilibrium [1][2]. The net radial self-force on the beam electrons scales as $(\gamma^2 f)$ where γ is the Lorentz factor and f is the ratio of the ion charge density to the electron charge

density [3]. Thus, a relatively small ion charge density can upset the beam equilibrium for high- γ beams that are weakly magnetized. Ions in the beam channel can also lead to instabilities such as the ion-hose instability [4] further degrading the beam.

On the second axis of DARHT, there are number of places where beam interception is expected. These range from regions where low charge densities are deposited such as beam clean-up apertures and the kicker septum (a few tens of nC/mm², 2000 ns time scale) to the areas with much higher charge density such as the target (few thousand nC/mm², 10-100 ns time scale). To study these effects, we have used the first axis DARHT beam as a probe. The beam is focused onto a thin foil (or mesh) to minimize the beam scattering. The mean current density can be varied over a wide range (from 0.5A/mm² to 100A/mm²) with an upstream focusing magnet. The time-dependent behaviour of the beam radial profile is observed some distance downstream to assess the effects of ion release, from the foil or mesh, on the beam dynamics. The observations are compared with Particle-In-Cell (PIC) computer modelling to study ion emission at the foil (mesh).

The paper is organized as follows: First, description of the experimental configuration and the particle-in-cell computational technique are presented. Next, major experimental results of the beam disruption for various materials as a function of current density are compared with the results of computer calculations. The paper concludes with a summary and discussion of on-going experiments.

2 EXPERIMENTAL SET-UP AND PIC CODE

2.1 Beam line and diagnostics

The DARHT first axis accelerator is an induction LIA composed of a 4 MV injector (1.7kA, 80ns) and 64 induction cells (250kV maximum each). The set-up used for the experiment described here (cf. Figure 1) is located after the last induction cell where the beam energy is 19.8 MeV. This part of the beam line consists of two cryogenic pumps able to establish a vacuum better than 2×10^{-6} Torr, three Beam Position Monitors (BPM), a spinning wheels system that prevents target debris from

damaging the accelerator, a magnetic solenoid, a foil chamber, a diagnostic section, and a beam stop.

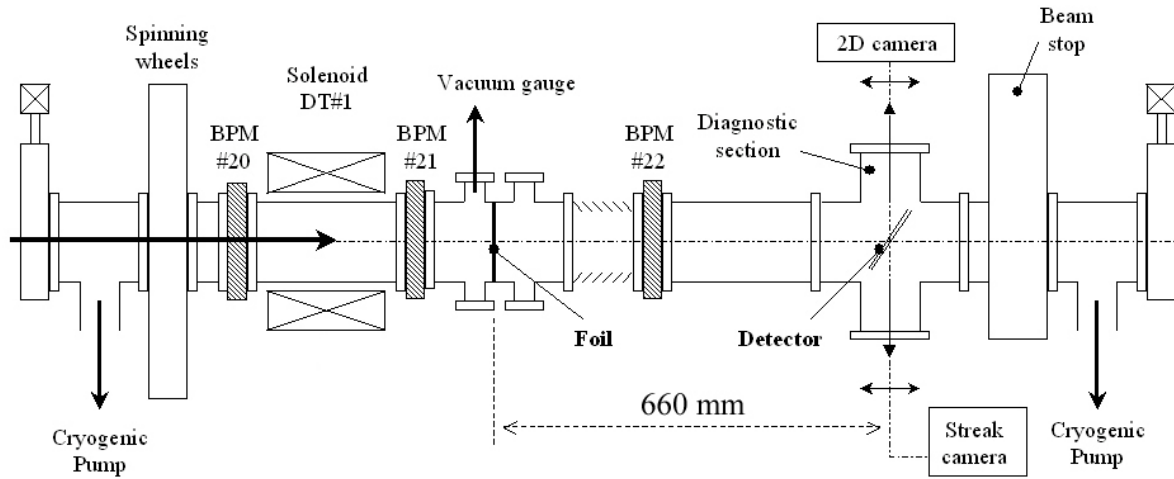


Figure 1: The experimental set-up (not to scale).

The beam-focusing solenoid, DT#1, allows the mean beam current density at the foil to be adjusted from 0.5A/mm^2 to 100A/mm^2 . Figure 2 shows the Root Mean Square (RMS) beam radius at the foil location for different DT#1 currents. The experimental results (symbols) are compared with beam envelope code predictions (lines).

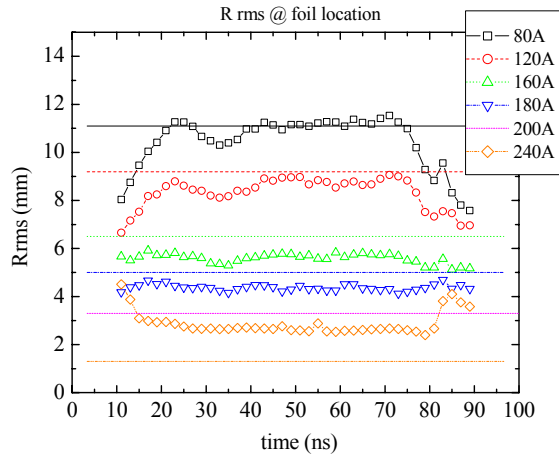


Figure 2: RMS beam radius versus time at the foil location for different DT#1 solenoid currents.

The beam current is constant between $t=20\text{ ns}$ and $t=80\text{ ns}$ as expected since the beam energy is constant to 1 % over this time. The measurements and calculations show good agreement for $r > 3\text{ mm}$. For smaller beam radius, the measured beam radius is a factor of two larger than the calculated radius. This discrepancy can be explained in part by the $\sim 1\text{ mm}$ spatial resolution of the diagnostic. The stainless steel foil chamber has eight ports around the foil location for insertion of diagnostic devices. The foil is placed normal to the accelerator axis with the holder providing a symmetric return current connection. All the foils tested are listed in the Table 1.

The meshes are listed in the Table 2. No special precautions or preparations were applied to the foils before insertion in the beam line.

Table 1: List of the foils tried.

Material	Thickness (μm)	Mean scattering angle (mrad.)
Graphite	66	10.4
Aluminium	(a) 7.6 (b) 30	(a) 5.1 (b) 10.3
Titanium	12.7	10.5
Steel	3.8	8.1
Molybdenum	12.7	23.5
Tantalum	1.5	10.8
Gold	1.5	12.4

Table 2: List of the meshes tried.

Material	Wire diameter (μm)	Open area (%)
Titanium	51	60
Tungsten	51	90

The three-part detector located 660 mm downstream of the foil is composed of a thin ($10\text{ }\mu\text{m}$) aluminized Kapton foil, a graphite disk (1 mm thick), and a 1 mm diameter quartz fiber placed vertically through the beam axis. This detector is tilted 43.6° with respect to the accelerator axis to image the Optical Transition Radiation (OTR) produced at the vacuum-aluminium interface with a 500 ms exposure camera. This camera detects the time average beam distribution. A streak camera images the “Cerenkov” radiation from the fiber yielding the beam radial profile versus time. The three BPM’s (placed before and after DT#1 and between the foil and the detector) measure the total current and the beam centroid position versus time. A 94 GHz microwave interferometer measures transient plasma density at 3 cm from the foil surface. The microwave horns are positioned 13 cm apart with the transmission axis parallel

to the foil. Assuming the plasma is confined within a 1 cm radius of beam center, the interferometer is sensitive to average free-electron densities greater than 10^{10} cm^{-3} .

2.2 Particle-In-Cell code description

To model the beam-foil interaction, we used the parallelized 2-D/3-D particle-in-cell code Lsp [5]. The code has models for multiple scattering and energy-loss in materials, surface heating, particle emission from surfaces due to thermal and stimulated desorption, field emission, etc. For 2-D (r - z) calculations, the mesh-size near the axis of symmetry was approximately $\Delta r=0.05\text{cm}$, $\Delta z=0.15\text{cm}$. An explicit electromagnetic charge-conserving algorithm was used. We simulated the region from 55 cm upstream of the foil (which is in the downstream fringe-field of solenoid DT#1), to 75 cm downstream of the foil. An electron beam with a Gaussian profile was injected upstream. The foil was modelled as a conducting plane with scattering and energy-loss properties corresponding to $7.6 \mu\text{m}$ Al. Ions are allowed to emit at the space-charge-limited current density when the local foil temperature increase exceeded 300 K. Calculations were carried out for singly ionized H, C, and Al ions.

3 RESULTS ANALYSIS

3.1 Time delay on the ions production

Figure 4 displays the streak camera images recorded for different DT#1 currents.

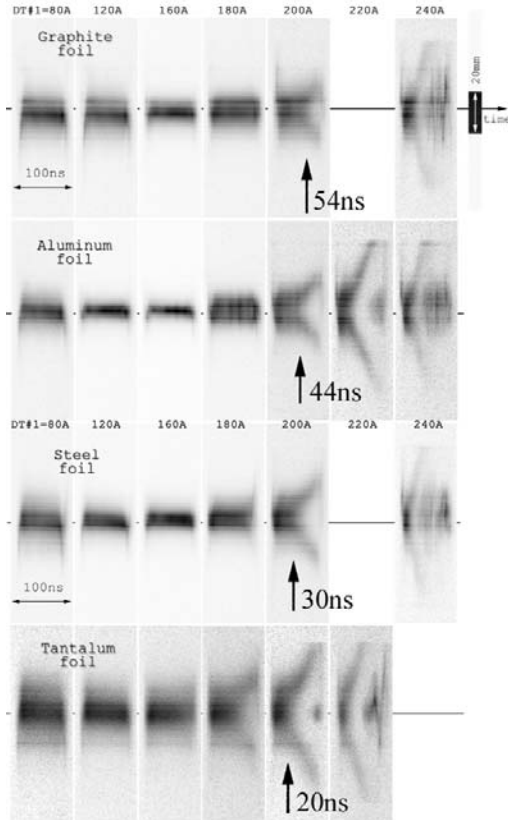


Figure 4: Streak camera images recorded for different DT#1 current setting and foil materials.

For simplicity only four foil materials are presented. Each frame (corresponding to a beam pulse) gives the vertical profile of the beam versus time. The spatial scale is indicated at the top right corner. Bright spots resulting from x-rays striking the streak camera CCD are removed by a post-treatment of the image. Some horizontal lines are present due to imperfections in the fiber. On each frame, a vertical line corresponds to the beam profile at a given time. By assuming beam axial symmetry, the time dependence of light collected can be compared with the beam current. This comparison provides a check to insure that the beam profile measurement is not influenced by beam motion in the horizontal direction. For each material there is a threshold value for the current density (given by the DT#1 current setting) at the foil. For current densities less than or equal to this value, the beam profile is constant over the 60 ns beam current plateau. In this case, the beam profile at the detector depends on the foil focusing effect [6] and foil scattering. Above this current density threshold, the beam profile becomes time dependent part way through the pulse. The delay for onset of this phenomenon is dependent on the foil material (cf. arrows on Figure 4). Assuming ion emission from the foil, this delay is the time needed for ions to be liberated and to propagate inside the beam channel.

Studies of anode plasma formation in diodes have produced strong evidence that a surface bombarded by an intense electron beam begins to emit ions after heating to $400 \pm 60^\circ\text{C}$ [7]. Others have proposed that ions from the foil material are generated after the foil material melts [8]. In the former model, the foil temperature rise leads to thermal desorption of impurities absorbed on the surface that are subsequently ionized [9]. Ionization can be due either beam impact or a cascade process in the high electric field at the foil surface. The impurities are typically water and hydrocarbons. The observed delay corresponds to the time needed to build a desorbed gas layer in front of the surface, the ionization time of the gas and the time for ions to move into the beam channel.

Table 3 shows the estimated time delays needed to heat the center of the foil to 400°C or to the melting point, for DT#1 currents of 200 A and 240 A.

Table 3: Time delay (ns) to heat foils to 400°C or melting.

Material (Melting temp. in deg. $^\circ\text{C}$)	DT#1=200A (50A/mm 2)		DT#1=240A (320A/mm 2)	
	400 $^\circ\text{C}$	melt	400 $^\circ\text{C}$	Melt
Graphite (3352)	52	> 200	8	125
Aluminum (6959)	44	80	7	12
Steel (1535)	26	160	4	25
Tantalum (3020)	8	70	1	11

These estimations are based on the temperature rise of the central part of a gaussian profile with the calculated RMS radius (cf. Section 2.1). We used the calculated radius because of the resolution limitations on the measured values for small radius. The delays needed to melt the foil are longer than the observed delays and in some case longer than the beam pulse. The delays need to reach 400°C are comparable to the measured delays. This indicates that ionization and ion motion is rapid or that the 400°C temperature is somewhat higher than the actual temperature for desorption.

No beam induced cleaning effects were observed. All data, including the first shot after installation, were reproducible. The beam produced holes at the beam center in all foils and meshes at on-axis current densities above 160 A/mm². After the expansion, the beam radius comes back to its original value. During this phase, a transverse oscillation of the beam centroid grows from the noise level (~1 mm) up to 10 mm. Measurements with the interferometer showed that free-electron densities above the instrumental noise level of 10¹⁰ cm⁻³ were not observed prior to melting the foil.

3.2 Comparison with PIC simulations – Nature of the ions

The measured beam RMS radii versus time (DT#1=200 A) are presented on the Figure 5.

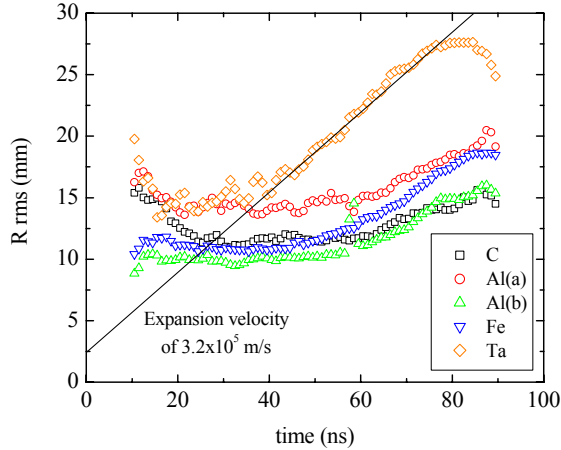


Figure 5: Beam RMS radius at the detector for different foil material (DT#1=200A).

After expansion begins, the time dependence of the beam radius can be approximated with a linear fit (constant expansion velocity). Computer calculations show this velocity depends on the mass of the ion emitted by the foil and the current density of the beam. For DT#1=200 A, PIC simulations assuming space charge limited emission give: 8.10⁵ m/s for H⁺ ions, 4.10⁵ m/s for C⁺ ions and 2.7 10⁵ m/s for Al⁺ ions. Independent of the foil material, experimental results range is from 2.6 to 3.2 10⁵ m/s. This comparison excludes very light ions (H⁺) and suggests a ratio of charge state to atomic weight

around 1/25. Many impurities molecules such as C₂H_m⁺, H₂O⁺, CO⁺, OH⁺, etc fall into this range.

3 Difference between a foil and a mesh

A highly transparent mesh could be placed in front of the foil to eliminate the longitudinal electric field responsible for ion acceleration. Of course, this idea will work only if ion production from the mesh is reduced relative to the target. To test this concept, a titanium mesh (90 % transparent) was tested and compared to the results from a titanium foil. The results are presented in Figure 6.

The difference in scattering between the mesh and the foil is clearly apparent in Figure 6. For the time-dependant part, there is not an important difference between the foil and the mesh. The beam disruption seems to be sooner with the mesh but this could be due to the difference in the scattering level. This comparison shows that there are enough ions available to reach the space-charge-limited current even when the frontal surface area is reduced by a factor of ten. This point validates the comparison made previously.

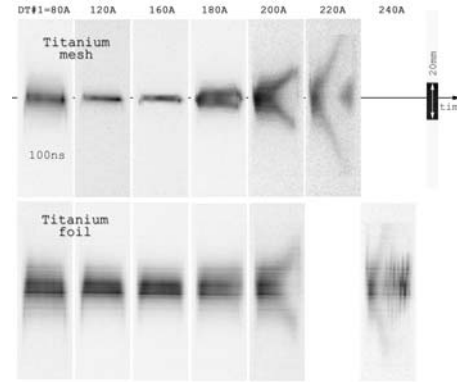


Figure 6: Comparison of the beam disruption induced by a foil and a mesh.

4 SUMMARY

Experiments and analysis presented support the ion emission from the foil induced by the beam. The charge to mass ratio of the ions emitted is independent of the foil material. Comparisons with PIC code suggest a charge to mass ratio around 1/25. The delays found to initiate this emission are consistent with the surface temperature reaching 400°C. On-going experiments will improve the resolution of the beam radius, include direct measurements of the ions present in the beam channel, and a time-resolved temperature measurement of the foil surface. 3D calculations to investigate the transverse oscillations are in progress.

REFERENCES

- [1] **D. R. Welch and T. P. Hughes**, Laser and Particle Beams, 16, 285, (1998).
- [2] **C. Vermare et al**, IEEE Transaction on Plasma Science, Vol. 27, #06, p. 1566, (1999).
- [3] **R. B. Miller**, *An Introduction to the Physics of Intense Charged Particle Beams*, Plenum Press, New York, p. 24, (1982).
- [4] **K. J. O'Brien**, J. Appl. Phys. **65** (1), p. 9, (1989).
- [5] **T. P. Hughes, R. E. Clark, and S. S. Yu**, Phys. Rev. ST Accel. Beams 2, 110401 (1999).
- [6] **R. F. Fernsler, R. F. Hubbard, and S. P. Slinker**, J. Appl. Phys. 68, 12, (1990).
- [7] **T. W. L. Sanford et al.**, J. Appl. Phys. 66, 10 (1989).
- [8] **T. J. Kwan et al.**, Phys. Of Plasmas, Vol. 7, #05, p. 2215, (2000).
- [9] **M. E. Cuneo**, IEEE Transaction on Dielectrics and Electrical Insulation, Vol. 6, #04, p. 469, (1999).